UCLA
UCLA Electronic Theses and Dissertations

Title

Nitrous acid (HONO) Chemistry over Snow in the Uintah Basin, Utah

Permalink

https://escholarship.org/uc/item/8d9136dq

Author

Li, Chengxi

Publication Date

2024

Peer reviewed|Thesis/dissertation

UNIVERSITY OF CALIFORNIA

Los Angeles

Nitrous Acid (HONO) Chemistry over Snow

in the Uintah Basin, Utah

A thesis submitted in partial satisfaction

of the requirements for the degree Master of Science

in Atmospheric and Oceanic Sciences

by

Chengxi Li

2024

ABSTRACT OF THE THESIS

Nitrous Acid (HONO) Chemistry over Snow

in the Uintah Basin, Utah

by

Chengxi Li

Master of Science in Atmospheric and Oceanic Sciences

University of California, Los Angeles, 2024

Professor Jochen Peter Stutz, Chair

OH radicals are crucial for the formation of secondary organic aerosol (SOA) and ozone in the atmosphere. HONO photolysis is one of the main sources of OH radicals, especially in winter. HONO chemistry in polluted areas has been a widely discussed in the last five decades. However, HONO chemistry is often absent or simplified in air quality models, making its impact on OH radical chemistry uncertain. In this thesis, I investigated the formation of HONO over snow in a polluted rural area.

The platform for atmospheric chemistry and vertical transport in one dimension (PACT-1D) model was used to calculate a 4-day cycle (Jan. 18th -Jan. 21st,2014) of atmospheric composi-

tion and HONO figures. The model output was compared with observational data from the Uintah Basin Winter Ozone Study 2014(UBWOS 2014). Modeled HONO mixing ratios compared well with observation. HONO fluxes from surface chemistry in the model shows good agreement of shape and magnitude.

In conclusion, PACT-1D model calculations show that chemical HONO formation on the snow explain the observed HONO mixing ratios.

The dissertation of Chengxi Li is approved.

Marcelo Chamecki

Suzanne E. Paulson

Jochen Peter Stutz, Committee Chair

University of California, Los Angeles

2024

TABLE OF CONTENTS

LIST OF FIGURES

LIST OF TABLES

ACKNOWLEDGEMENT

I'd like to express my gratitude to my advisor and my committee chair, Professor Jochen P. Stutz, for his patient guidance. I hope our scientific cooperation will continue. I would like to express my thank to the rest of my committee: Prof. Suzanne E. Paulson and Prof. Marcelo Chamecki for their support. I also owe acknowledgement to Catalina J. Tsai for providing UBWOS 2014 field data analysis and Jennie L. Thomas for providing access to PACT-1D model. Your sharing is significant to my studies. Last but not least, I want to express my thanks to my parents for their support that allowed me to finish my thesis.

1. INTRODUCTION

The hydroxyl radical (OH) is one of the most important oxidizing species in the atmosphere.

The OH radical reacts with organics at their carbon-carbon unsaturated bonds, substitutes on aromatic rings, or undergoes monoelectronic oxidation of organics (Gligorovski et al., 2015).

OH radical is crucial for the formation of ozone and secondary organic aerosols (SOA).

OH can produce HO_2(R1-R2) to maintain the OH-HO_2 balance:

$$OH + CO + O_2 \rightarrow HO_2 + CO_2 \qquad\qquad \text{(R1)}$$

$$OH + VOC \rightarrow HO_2 + compounds \qquad\qquad \text{(R2)}$$
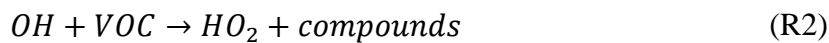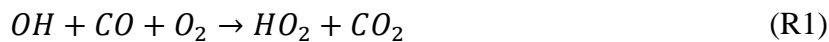
And the HO_2 radical produces NO_2 (R3):

$$HO_2 + NO \rightarrow OH + NO_2 \qquad\qquad \text{(R3)}$$

Produced NO_2 will thus form ozone as in R4-R5:

$$NO_2 + hv(\lambda < 420nm) \rightarrow NO + O(^3P) \qquad\qquad \text{(R4)}$$

$$O(^3P) + O_2 \rightarrow O_3 \qquad\qquad \text{(R5)}$$
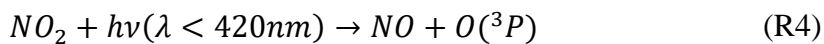
This illustrates how the OH radical is involved in ozone production.

There are various methods of producing OH in the air. According to Rohrer and Berresheim (2006), in the troposphere, OH is produced primaily by ozone photolysis (R6-R7):

$$O_3 + hv(\lambda < 330nm) \rightarrow O(^1D) + O_2 \qquad\qquad\text{(R6)}$$

$$O(^1D) + H_2O \rightarrow 2OH \qquad\qquad\text{(R7)}$$
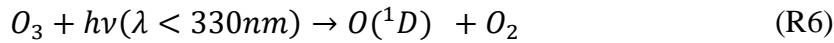
A second source of OH is formaldehyde (HCHO) photolysis (R8-R11) followed by HO_2+NO reaction (Meller & Moortgart, 2000):

$$HCHO + hv(\lambda < 370nm) \rightarrow H + HCO \qquad\qquad\text{(R8)}$$

$$\rightarrow H_2 + CO \qquad\qquad\text{(R9)}$$

$$H + O_2 \rightarrow HO_2 \qquad\qquad\text{(R10)}$$

$$HCO + O_2 \rightarrow HO_2 + CO \qquad\qquad\text{(R11)}$$

$$HO_2 + NO \rightarrow OH + NO_2 \qquad\qquad\text{(R3)}$$
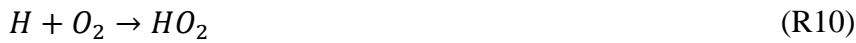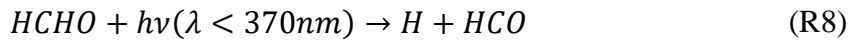
Alkenes also serve as significant OH sources while reacting with ozone (Paulson et al., 1999).

Nitrous Acid (HONO) photolysis (R13) is another significant source of OH radicals (Tuite et al., 2021; Alicke et al., 2003).

$$HONO + hv(< 440\ nm) \rightarrow OH + NO \qquad\qquad\text{(R12)}$$
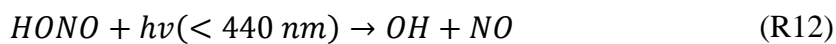
Therefore, HONO chemistry in polluted areas has been a widely researched topic in the last half-century. However, HONO chemistry is usually not included or is included in a simplified way in air quality models, which leads to its concentration being underestimated. Consequently, this underestimation will also affect the prediction of secondary pollutants' concentrations like ozone.

1.1 HONO Formation and Loss Mechanisms

The main gas reactions of gas-phase HONO besides its photolysis(R12), are R13 and R14:

$$HONO + OH \rightarrow NO_2 + H_2O \qquad\qquad\qquad (R13)$$

$$OH + NO \xrightarrow{M} HONO \qquad\qquad\qquad (R14)$$

Measured diurnal profiles show that HONO accumulates at nighttime, but once the photolysis rate increases in the day, its concentration drops. The highest level of HONO is measured in polluted areas near the ground at night, which mixing ratios reaching several parts per billion (ppb) (Kleffmann et al., 2006; Stutz et al., 2010; Wong et al., 2011), while the missing ratio is a few hundred parts per trillion (ppt) during the day (Acker et al., 2006; Kleffmann et al., 2005; Wong et al., 2012; Zhou et al., 2007).

Pseudo-Steady State (PSS) calculations show that these numbers are greatly underestimated when only homogeneous chemistry (R12-R14) is applied. Anthropogenic emissions only contribute less than 1% of NO_x emissions (Kirchstetter et al., 1996; Kramer et al., 2019; Kurtenbach et al., 2001; Neuman et al., 2016). Therefore, heterogeneous formation must be taken into consideration.

HONO can be converted from NO_2 in reactions on moist surfaces (R15), which is the main source of nocturnal HONO and can accurately describe HONO and NO_2/HONO ratios at night:

$$2NO_2 + H_2O \xrightarrow{surface} HONO + HNO_3 \qquad\qquad (R15)$$

This mechanism is first order in [NO$_2$].

There are several possible proposed HONO formation mechanisms:

1. Formation on surfaces from absorbed nitric acid: This process, outlined in R16-R19 (Zhou et al., 2002) and depicted in Figure 1.2, involves the conversion of HNO$_3$ absorbed on surfaces. HONO produced in reactions R17 and R19 can quickly transition into the gas phase, which is significant for daytime HONO formation in environments with low NO$_2$ levels. This enhanced photolysis likely plays a role in urban HONO production (Tuite et al., 2021).

$$HNO_{3(ads)} + h\upsilon \rightarrow [HNO_3]^*_{(ads)} \hspace{4cm} (R16)$$

$$[HNO_3]^*_{(ads)} \rightarrow HONO_{(ads)} + O(^3P) \hspace{3cm} (R17)$$

$$[HNO_3]^*_{(ads)} \rightarrow NO_{2(ads)} + OH \hspace{3.5cm} (R18)$$

$$2NO_{2(ads)} + H_2O \rightarrow HONO_{(ads)} + HNO_{3(ads)} \hspace{2cm} (R19)$$
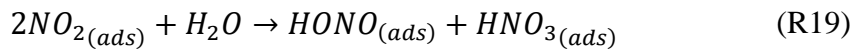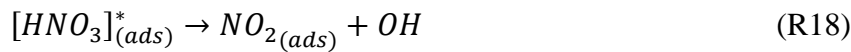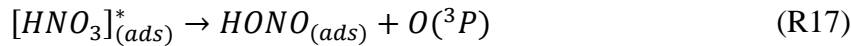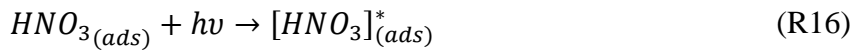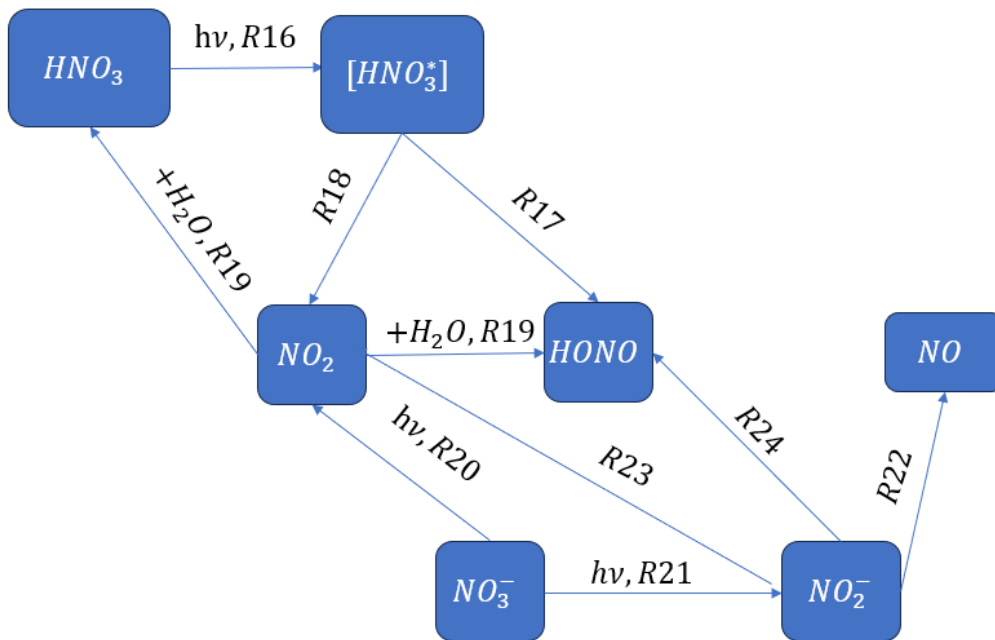
Figure 1.1 HONO Formation Mechanisms (Including Formations Over Snow)

2. Photo enhanced NO_2 reduction: R15 is insufficient to maintain HONO levels during the day, so a photolytic source is required. This mechanism occurs both at organic surfaces (Kleffmann, 2007) and within a Quasi-Liquid Layer (QLL). According to Stemmler et al. (2006) and Zhou et al. (2003), the reaction rate of NO_2 formation to HONO is positively proportional to NO_2 concentration, irradiance (I), and surface area (SA) (1):

$$P_{HONO} \propto SA \times [NO_2] \times I \qquad (1)$$

This will be discussed in more detail in Section 1.2.

3. Gas-phase photolysis of organic nitrates: Observed in a chamber study conducted by Rohrer et al. (2005).

4. Soil bacteria: Oswald et al. (2013) quantified soil emission of HONO. However, this mechanism can be disregarded because the snow-covered ground is too cold for bacteria to be active.

1.2 HONO Formation Over Snow

HONO emission from snow has been observed across a wide range of locations on Earth. According to Honrath et al. (1999), the levels of HONO and NO_x are significantly higher (3 to >10 times) in the interstitial air of surface snow compared to ambient air at the summit of Greenland. Other studies conducted at high latitude sites (Beine et al., 2002; Dibb et al., 2002; Jacobi et al., 2004) have concluded that snow, once exposed to air, releases NO_x into the air. Additionally, according to Amoroso et al. (2006) and Beine et al. (2006), snow provides HONO via photolysis. However, no significant increase in HONO levels was detected in places where snow is alkaline.

As discussed in Section 1.1, the mechanism of snow formation involves nitrate photolysis (R21-R25) (Chu & Anastasio, 2007; Jacobi & Hilker, 2007):

$$NO_3^- \xrightarrow{h\upsilon > 290nm} NO_2 + O^- \qquad\qquad \text{(R21)}$$

$$NO_3^- \xrightarrow{h\upsilon > 290nm} NO_2^- + O(^3P) \qquad\qquad \text{(R22)}$$

The NO_2^- produced in R22 can generate NO via photolysis (R23) and react with OH, resulting in generation of NO_2 (R24) (Chu & Anastasio (2007); Jacobi & Hilker (2007):

$$NO_2^- \xrightarrow{h\nu} NO + O^- \qquad\qquad\qquad \text{(R23)}$$

$$NO_2^- + OH \rightarrow NO_2 + OH \qquad\qquad\qquad \text{(R24)}$$

And generate HONO followed by R16.

Also, under the circumstances of acid/base equilibria for liquid water applicable to snow, NO_2^- can be protonated, producing HONO (R25):

$$NO_2^- + H^+ \rightarrow HONO \qquad\qquad\qquad \text{(R25)}$$

HONO is then rapidly returned into the gas phase.

Laboratory experiments and field studies have found that the reaction of HONO and NO_x occurs at the air-ice surface, also known as the Quasi-Liquid Layer (QLL) (Döppenschmidt & Butt, 2000). According to Chu and Anastasio (2007), the temperature dependence of NO_3^- quantum yield efficiency remains consistent in solution and ice, indicating that NO_3^- photolysis occurs at the QLL.

Recent laboratory studies show other possible mechanisms of HONO formation over snow. According to George et al. (2005), the reduction of NO_2 by photosensitized organics is also a possible mechanism. Beine et al. (2008) assert that the HONO flux produced by NO_2 reduction (R12) has a strong positive correlation with the HULIS (humic-like substances) content of the snow surface, which is also a possible mechanism of HONO formation over snow. However, according to Grannas et al. (2007), further research is needed to fully understand the HONO production mechanism.

1.3 HONO Measurements Over Snow

Table 1 shows different studies of HONO concentrations over snow:

Study	HONO mixing ratio
V. Michoud et al., 2014	5-10 pptv
Chen et al., 2019	54±41 pptv
Legrand et al., 2014	20-40 pptv
Zhou et al., 2001	6.1±1.4 pptv
Spataro et al., 2017	8.33 ppt(mean)/37.93 ppt(max)

Table 1 HONO Concentration Observation Over Snow in Different Studies in pole regions

According to Table 1, HONO mixing ratio over snow in clean areas is around tens ppt in mixing ratio with a maximum of 95 pptv (Chen et al., 2019).

Polar HONO measurements have been challenging due to conflicts between measurements of HONO, NO_x, and HO_x (Grannas et al., 2007). According to Chen et al. (2001), during the ISCAT 1998 study, mist chamber measurements of HONO yielded concentrations of about 30 parts per trillion by volume (pptv). However, these measurements exhibited an overestimation of OH by a factor of 2 to 5, casting doubt on the validity of mist chamber measurements. Furthermore, Grannas et al. (2007) highlighted that during the 2004 Greenland studies, HO_2 + RO_2 measurements agreed well only when HONO was not included, further raising concerns about the accuracy of HONO measurements.

On the other hand, Zhou et al. (2002) discovered that a photochemical source of HONO could make it the dominant source of OH in boundary layers. These findings are consistent with model results reported by Grannas et al. (2002) despite the model's inadequate performance in predicting HO_x emissions.

1.4 HONO Measurement Techniques

There are various ways of measuring HONO. This section will give a brief introduction of these ways and discuss the technique used in this thesis.

<u>Incoherent Broad Band Cavity-Enhanced Absorption Spectroscopy (ACES or IBBCEAS)</u>

IBBCEAS utilizes UV absorption within a cavity to measure HONO concentrations. This technique employs two highly reflective mirrors to trap light, thereby increasing the effective absorption path length. Data retrieval involves analyzing absorption spectra resulting from light transmission within the cavity with or without absorbing species (Wu et al., 2012). Min et al. (2016) provided detailed insights into this technique in a study measuring aircraft HONO, reporting a detection limit of ~200 ppt for HONO.

<u>Chemical Ionization Mass Spectroscopy (CIMS)</u>

CIMS involves chemically ionizing HONO molecules using a reagent, enabling mass spectrometers to analyze and identify HONO. HONO is ionized through an iodide ion transfer reaction (iCIMS or Iodide Chemical Ionization Mass Spectrometry) or a negative proton

transfer reaction. This technique achieves high sensitivity (~15-20 pptv) and high time resolution (1s) (Roberts et al., 2010).

Long Path Absorption Photometry (LOPAP)

LOPAP is commonly employed in polar HONO observations. It directly samples gas-phase HONO in a stripping coil using in-situ wet chemical instruments. The stripping reagent is converted to an azo dye, eliminating the need for sampling lines and minimizing surface sampling artifacts. The equipment uses a light-emitting diode and measures absorption in long-path absorption tubes. Two stripping coils are utilized to detect HONO presence an-didentify possible interferences (first coil) and quantify HONO (second coil). By measuring the difference between the two channels, the HONO signal is determined (Kleffmann et al., 2002; Pinto et al., 2014).

Differential Optical Absorption Spectroscopy (DOAS)

The field data used in this research is obtained from UCLA Long Path Differential Optical Absorption Spectroscopy (LP-DOAS) instrument. DOAS measures HONO by quantifying its absorption structures in the UV spectral region. DOAS separates absorption spectra into narrowband and broadband absorptions, enabling the calculation of species concentration based on absorption bands depths (Platt & Stutz, 2008).

<u>Theory of DOAS</u>

DOAS relies on Beer-Lambert's law, represented by equation (2):

$$I(\lambda) = I_0(\lambda) * \exp(-\sigma(\lambda, T) * c * L) \qquad (2)$$

Where $I_0(\lambda)$ is the original intensity of the light source, $I(\lambda)$ is the intensity of the light after passing a length of L, c is the concentration of the absorber and σ denotes the absorption cross-section of the absorber.

Beer-Lambert's law states that intensity decays exponentially with distance, and the concentration of the absorber gas can be calculated. However, measuring $I_0(\lambda)$ can be challenging. Dividing the spectrum into broadband and narrowband structures helps address this challenge.

Substituting $\sigma(\lambda, T)$ with the sum of low frequency part $\sigma_{j0}(\lambda, T)$ and high frequency part $\sigma_j'(\lambda, T)$ in equation 2, allows calculation of a broadband spectrum $I_0'(\lambda)$.

The concentrations of trace gases can then be calculated using equation (3):

$$c_j = \frac{\ln\left(\frac{I_0'(\lambda)}{I(\lambda)}\right)}{\sigma_j'(\lambda, T) * L} \qquad (3)$$

1.5 HONO Fluxes over snow

HONO fluxes describe the amount of HONO emitted from a snow surface per second. Most HONO fluxes measurements follows the gradient method proposed by Businger (1986):

$$F_C = -K_C \frac{dC}{dz} \qquad (4)$$

Where K_C is the eddy diffusivity coefficient and $\frac{dC}{dz}$ is the vertical gradient of the HONO concentration.

The eddy diffusivity coefficient K at a specific height Z, according to Businger (1986), can be calculated using equation (5):

$$K = \frac{\chi \times u^* \times (Z - D)}{\Theta\left(\frac{Z}{L}\right)} \qquad (5)$$

Where χ is the Von Karman constant (0.37) (Telford & Businger, 1986), L is the Monin-Obukhov length, $u*$ is the friction velocity, and D is the displacement height. $\Theta\left(\frac{Z}{L}\right)$ represents the dimensionless wind shear, calculated as follows in equation (6):

$$\Theta\left(\frac{Z}{L}\right) = \left(1 - \frac{16(Z-D)}{L}\right)^{-\frac{1}{2}}, \frac{Z}{L} < 0 \ (unstable\ condition)$$

$$\Theta\left(\frac{Z}{L}\right) = \left(1 + \frac{5(Z-D)}{L}\right), \frac{Z}{L} > 0 \ (stable\ condition) \qquad (6)$$

The displacement height D, as per Stanhill (1969), can be estimated using the zero-plane displacement height equation (equation (7):

$$\log(D) = 0.9793 \log(h) - 0.1536 \qquad (7)$$

Where h is vegetation height.

Once the observation data is retrieved, fluxes can be calculated using the aforementioned method. Table 2 presents some results from the calculation of HONO flux over snow.

Study	Mean HONO vertical flux ($molec\ cm^{-2}s^{-1}$)
Honrath et al. (2002)	3.1×10^7
Beine et al. (2008)	$3 \times 10^{10}(NO + NO_2 + HONO)$
Beine et al. (2006)	1.67×10^8
Spatato et al. (2017)	2.18×10^8
Bond et al. (2023)	3.4×10^8

Table 2 HONO Fluxes Over Snow in Various Studies

Table 2 gives typical values of HONO flux at about $10^8\ molec\ cm^{-2}s^{-1}$.

1.6 Motivation

Previous studies have utilized both observational data and laboratory results to explore potential mechanisms of HONO formation over snow surfaces. However, these studies have often lacked the integration of model results with observational data, particularly concerning HONO emissions over snow. Consequently, differences and agreements between model predictions and observations remain unclear. This study aims to address this gap by combining observation data and model results to quantify HONO emissions over snow surfaces.

This thesis aims to address the following questions:

- What are the mechanisms underlying HONO formation over snow surfaces?

- Can we accurately model HONO and HONO fluxes over snow?

2. METHODOLOGY

This chapter will provide a brief overview of the methodology employed and the input data utilized in this study. Specifically, it will introduce the Platform for Atmospheric Chemistry and Vertical Transport in One Dimension (PACT-1D) model, along with the input file compiled from the Uintah Basin Winter Ozone Study (UBWOS) data.

2.1 Platform for Atmospheric Chemistry and Vertical Transport in One Dimension (PACT-1D)

PACT-1D was utilized to solve one-dimensional transport and chemical kinetics for a specific chemical species i at a given height z and time t. The continuity equation is represented as follows (equation 7; Figure 2.1) (Tuite et al., 2021):

$$\frac{dC_{i,t,z}}{dt} = P_{i,t,z} - L_{i,t,z} + E_{i,t,z} + F_{i,t,z} \tag{7}$$
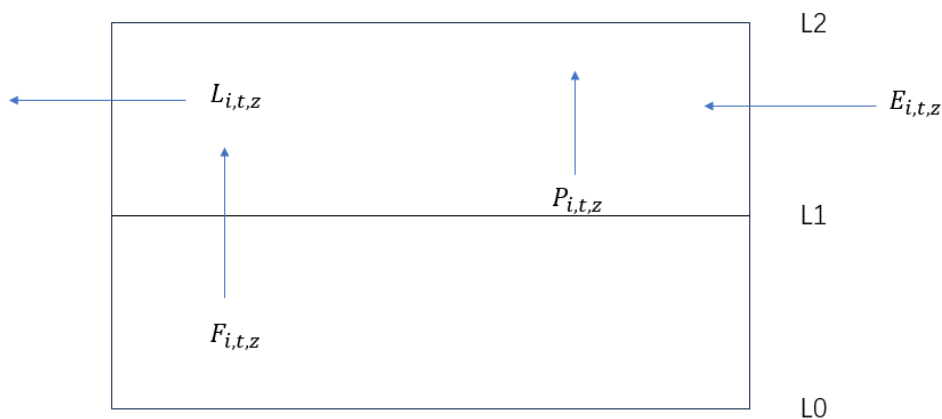

Figure 2.1 The Continuity Equation

Where C is the concentration of species, P stands for production and L stands for loss, F is flux contribution and E is emission rate.

Emissions are dependent on both time and height. The Regional Atmospheric Chemistry Mechanism version 2 (RACM2) (Goliff et al., 2013) is employed to describe chemical production and loss within the model, along with the Kinetics Pre-Processor (Sandu & Sander, 2006). The model incorporates the non-reactive uptake of gases to aerosols and heterogeneous reactions on aerosol surfaces. The aerosol surface area is calculated using equation 8:

$$S = 4\pi r^2_{(z,t)} N_{(z,t)} \tag{8}$$

Where r and N denote the radius and number concentration of aerosols at a specific height z and time t.

The irreversible uptake to aerosol surfaces and the heterogeneous reaction rate constant K_T are determined by (9):

$$K_T = \frac{1}{4} v S \gamma J \tag{9}$$

Where v stands for molecular speed, S is the surface area calculated in (8), γ is the possibility of irreversible uptake or reaction on surface. J is the flux of molecule to the aerosol surface, which can be calculated using the method of Fuchs and Sutugin (1971).

Vertical mixing and ground loss are included in the vertical mixing equation

$$\frac{\delta}{\delta t} \Phi_{(i,t,z)} = \frac{1}{\rho_{(i,t,z)}} \frac{\delta}{\delta z} \left(\rho_{(i,t,z)} K_{D(i,t,z)} \frac{\delta}{\delta z} \Phi_{(i,t,z)} \right) + R_{(1,t)} \tag{10}$$

In equation (10), Φ_i is the species mixing ratio, ρ is air density, R is the ground loss to the lowest box of the model, K_D is eddy diffusivity plus molecular diffusion.

The surface loss of each species is included in equation (10):

Ground loss R is calculated based on molecular collisions with the ground and combined with uptake probability (or reactive uptake efficiency).

This method allows the calculation on surface-level molecular reactions; thus, a deposition velocity does not have to be prescribed. Deposition rates are calculated when solving equation (10). Interactive surface chemistry is also included, which releases ground species into the gas phase.

The boxes which are lower than 1m are displayed in log scale so that the lowest boxes are small enough for treating a laminar diffusion layer contacting on earth surface directly.

2.2 Uintah Winter Basin Ozone Study (UBWOS)

The Uintah Basin Winter Ozone Study (UBWOS) was a comprehensive field study conducted during the 2012-2014 winter seasons. It primarily focused on identifying emission sources and photochemical processes contributing to increased ozone formation in winter, with the aim of mitigating ozone pollution (Tsai, 2016).

This study specifically delves into the results obtained during UBWOS 2014; a follow-up study conducted during the winter of 2013-2014. UBWOS 2014 aimed to acquire reliable and representative measurements of HONO using various techniques.
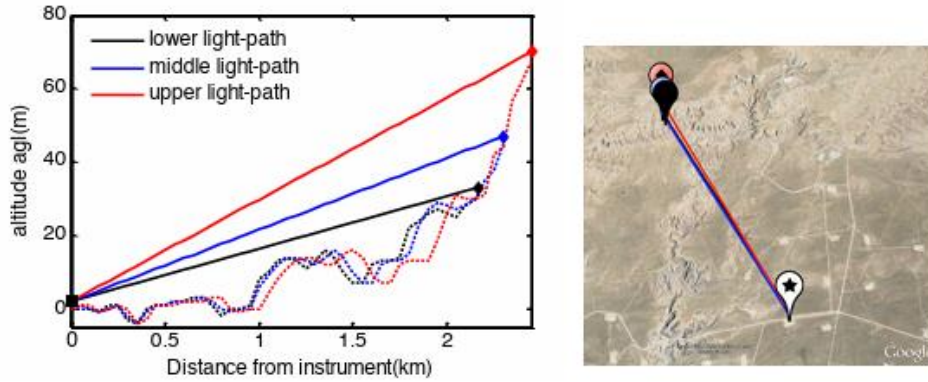
Figure 2.2 UCLA LP-DOAS Equipment Setup (Tsai, 2016)

Figure 2.2 is the setup of the UCLA LP-DOAS equipment during UBWOS 2014. The left panel shows the side view of the DOAS system, in this panel, the solid lines are light paths (lower, middle, upper), and dashed lines are local topography under the lines. The right panel shows the upper view of the light paths (Tsai, 2016).

UBWOS 2014 involved extensive observations of various species concentrations. Below are some of the data retrieved from LP-DOAS measurements, indicating species concentrations in parts per billion (ppb) (NOAA, 2014):
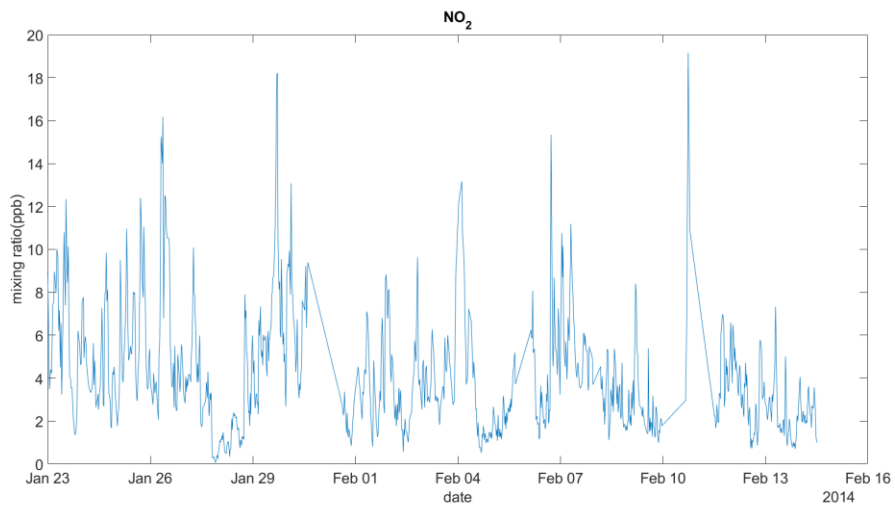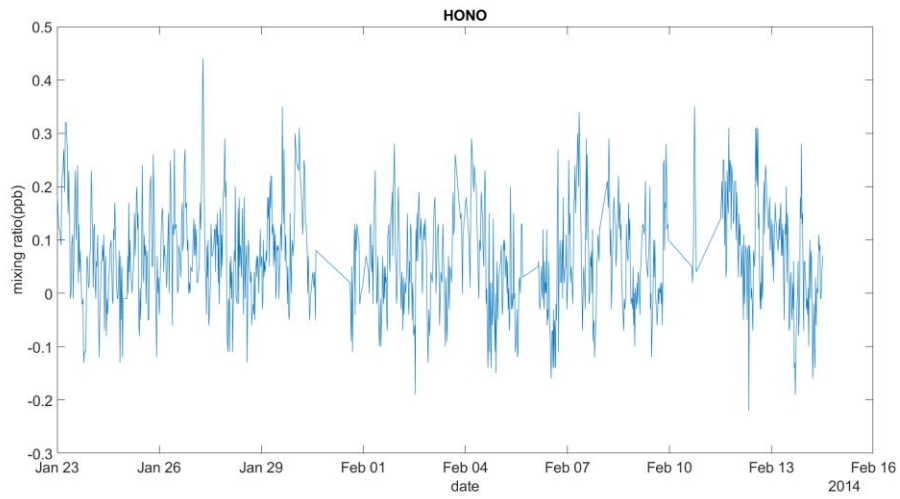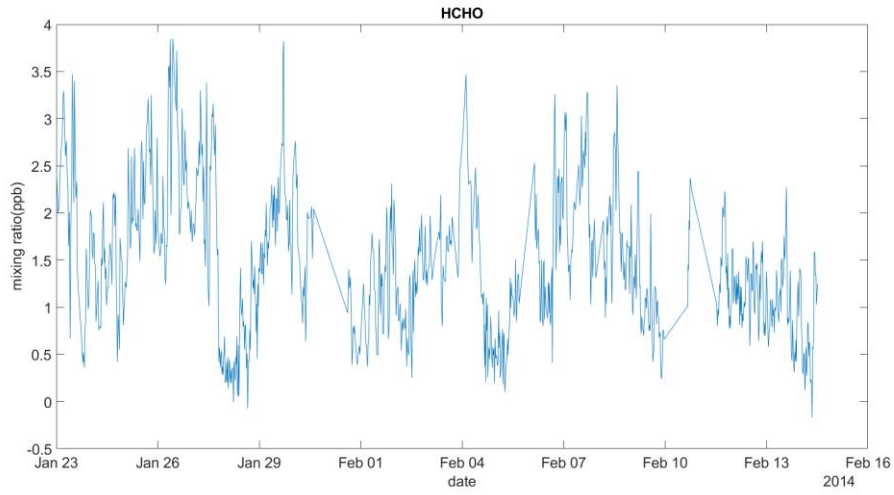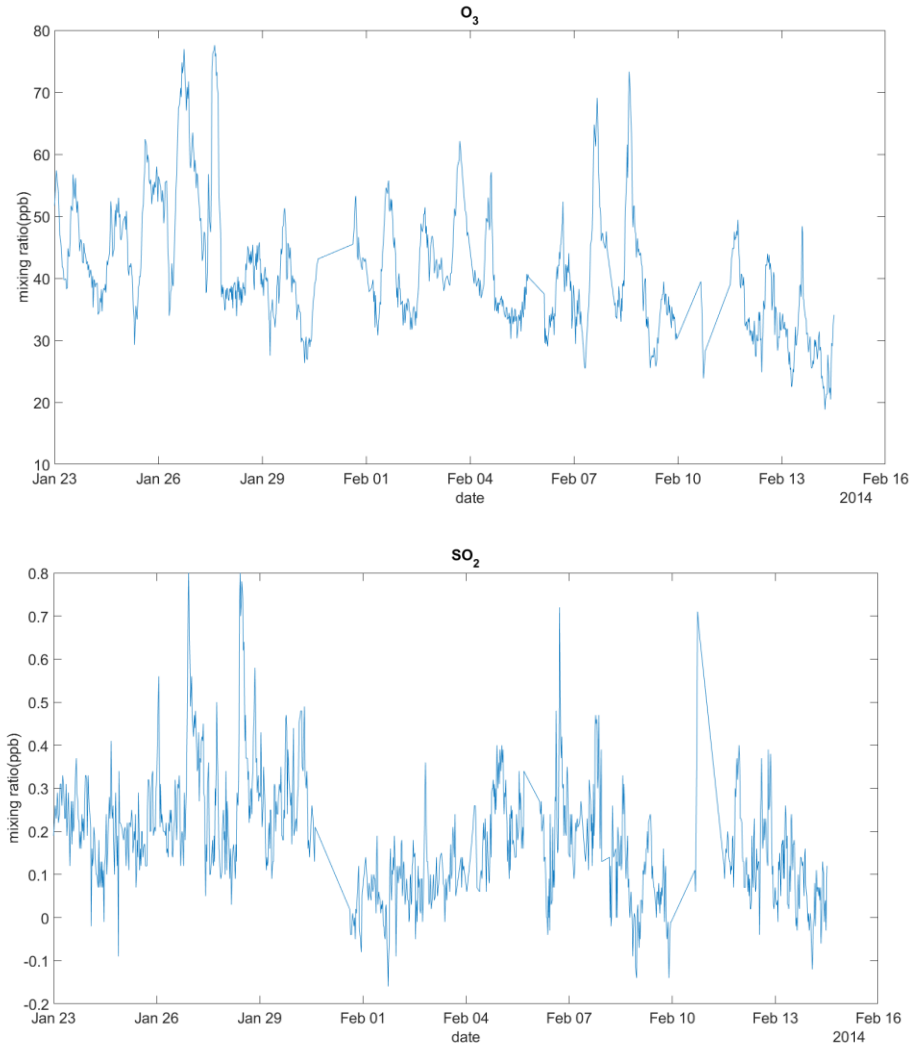
Figure 2.3 Observation Data of Species Concentration Retrieved from UBWOS 20

NO2 exhibited a concentration cycle of 3-4 days, with peaked around 15-20 ppb. The highest concentrations were observed on Jan. 30th Feb 11th, reaching approximately 20 ppb. HONO, conversely, maintained a relatively stable concentration around 0.2 ppb. The highest recorded HONO concentration was on Jan 27th, approximately 0.4 ppb. HCHO also displayed a concentration cycle of 4-5 days, with peaked around 3-4 ppb. The highest HCHO concentration occurred on Jan 30th, reaching about 4 ppb. Ozone(O3) demonstrated a cycle period of 1 day, primarily driven by solar activity and its reaction with NO. The highest concentration was

19

observed on Jan 27th and Feb 8th, approximately 80 ppb. SO$_2$ concentration did not exhibit a clear cycle, but it had peaks around 0.8 ppb. The highest SO$_2$ concentration was observed on Jan 27th and 29th, approximately 0.8 ppb. Feb. 7th and 11th also show lower peaks around 0.75ppb.

According to Tsai (2016), the daily average HONO vertical flux from observations using the method discussed in Section 1 is depicted in Figure 2.3.
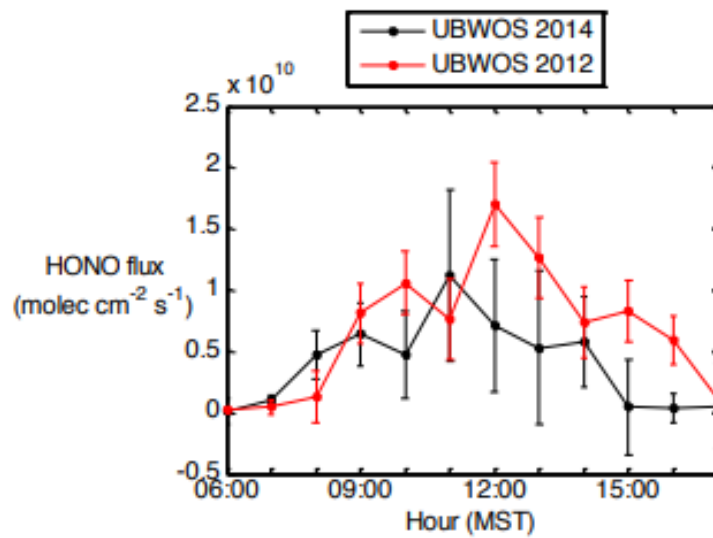

Figure 2.4 Daily HONO Flux Comparison of UBWOS 2014 and UBWOS 2012(Tsai, 2016)

The fluxes measured in UBWOS were 10 times larger than studies mentioned in section 1. On average sunny days, the HONO flux closely mirrored solar irradiance patterns in both UBWOS 2012 and UBWOS 2014. However, when comparing UBWOS 2014 to UBWOS 2012, the HONO flux values were lower. Specifically, the maximum HONO flux observed during UBWOS 2012 over bare soil was approximately $1.8 \times 10^{10} molec\ cm^{-2}s^{-1}$, where-as during UBWOS 2014, the maximum value was around $1.2 \times 10^{10} molec\ cm^{-2}s^{-1}$. Addi-

tionally, in UBWOS 2014, the peak flux occurred at 11:00 local time, which was one hour earlier compared to UBWOS 2012.

2.3 Model Setup

The input for the model includes aerosol properties, atmospheric conditions, emissions data, initial concentrations, photolysis frequencies (J values), and Eddy Diffusivities (K_Z values).

Aerosol

Aerosol are assumed to have a constant radius of 100nm and a number density of $100cm^{-3}$.

Atmospheric Properties (Pressure, Temperature, Relative Humidity)

Atmospheric pressure follows an exponential decay with height using Equation (11):

$$p = p_0 e^{-\left(\frac{h}{h_o}\right)}$$ (11)

Where p_0 is the ground air pressure (1013hPa), h is height (in meters), and h_0 is the average boundary scale height (7500m).

Temperature profiles were calculated using Equation (12), where T_s are observed surface temperatures (in Kelvin), h is height, and γ is the lapse rate (estimated to be 6K/km in boundary layer).

$$T = T_S - \gamma h$$ (12)

Relative humidity was calculated using Equation (13), where *TD* is observed dew point tem-

perature (in Celsius) and *T* is temperature (in Celsius) (Alduchov, O. A., and R. E. Eskridge,

1996):

$$\text{RH} = 100 \times \frac{\exp\left(\frac{17.625 \times TD}{243.04 + TD}\right)}{\exp\left(\frac{17.625 \times T}{243.04 + T}\right)} \qquad (13)$$

These temperature data were also retrieved from meteorological data collected during the

Uintah Basin Winter Ozone Study (UBWOS).

Emissions

Emissions were obtained from the 2014 Air Agencies Oil and Gas Emissions Inventory in

table 4 (Utah Department of Environmental Quality, 2017):

Particle	Uintah Emission (Ton/Yr)
NO_x	7858.00
CO	5857.58

Table 3 Used Input Emission Source

The data was converted from ton/year to $mol/(m^2 * s)$ and adjusted for the area of the Uin-

tah basin ($\sim 30000 \ km^2$). The area of the Uintah Basin varies depending on the source. In this

study, the approximation of "slightly more than 10,000 mi^2" (J. W. Hood, 1976) was utilized,

which translates to approximately 30,000 square kilometers.

So, the conversion is:

$$E = E_0/(365 \times 24 \times 60 \times 60 \times 30000 \times 10^6 \times m)$$

Where E_0 is the emission from previous research in tons/year, E is the corrected emission in $mol/(m^2 * s)$, and m is the molar mass of a certain particle in g/mol. For NO_x, the m equals to the average value of NO and NO_2, which is 38g/mol.

The emissions values are considered constant over time because they originate from stationary sources.

Initial Concentrations

Initial concentrations of species are obtained from UBWOS observation data, as shown in Table 5.

Particle	Mixing Ratio(ppb)
O_3	40
NO	0.01
NO_2	10
CO	335.8
HCHO	2
HNO_3	0.469
HONO	0.1

Table 4 Initial Input Values from UBWOS 2014

<u>photolysis frequencies (*J* Values)</u>

J values are generated using the Tropospheric Ultraviolet and Visible (TUV) Radiation Model developed by the University Corporation for Atmospheric Research (UCAR), and these values are interpolated with meteorological data from UBWOS 2014 observations. The input *J* values of NO_2 are illustrated in Figure 2.4:
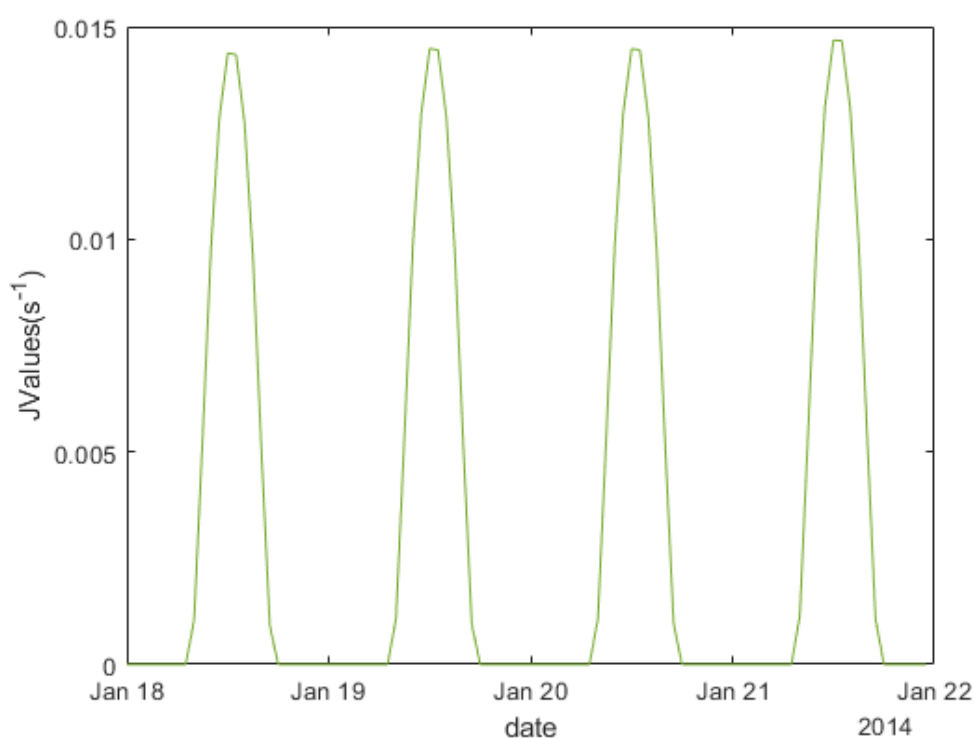

Figure 2.5 J Value of NO_2 During Jan-18 to Jan-21, 2014

The model output demonstrated agreement with diurnal cycles, and the peak values aligned closely (approximately $0.015s^{-1}$). To facilitate the TUV model's operation, the input ozone column values are obtained from the World Ozone and Ultraviolet Radiation Data Centre (WOUDC).

<u>Eddy Diffusivities (K$_Z$ Values)</u>

For K_Z values, I interpolated the output of the K_Z model from Geyer et al. (2004) to 26 layers

in the PACT-1D model and scaled it using the observation data on January 27, 2014(Tsai,

2016) and method described in section 1.5 (equation 5). The input K_Z values at different alti-

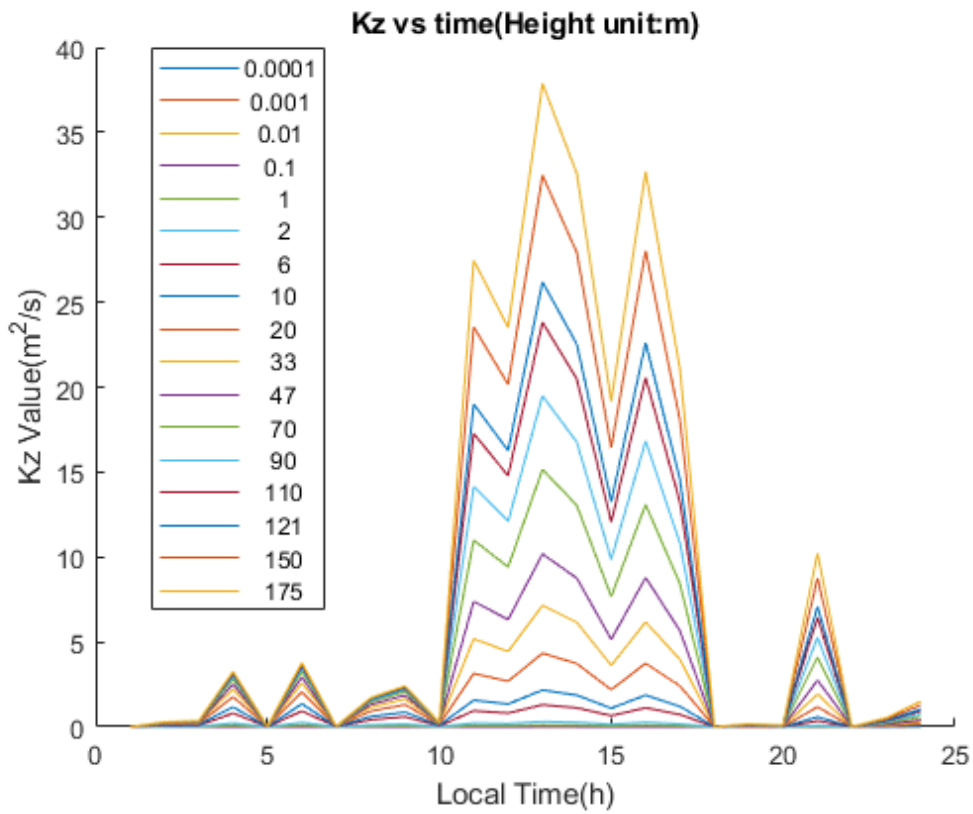tudes are shown in Figure 2.6:

Figure 2.6 Hourly K_Z Values Over Different Altitudes scaled by data on Jan 27th, 2014

We can see the K_Z values peak at 14:00 and are low at night.

<u>Vertical Grid</u>

Table 5 shows the 26-layer grid that PACT-1D is using:

Level	1	2	3	4	5	6	7	8	9
Height(m)	0.001	0.01	0.1	1	3	6	10	20	33
Level	**10**	**11**	**12**	**13**	**14**	**15**	**16**	**17**	**18**
Height(m)	50	78	90	110	121	150	175	255	300
Level	**19**	**20**	**21**	**22**	**23**	**24**	**25**	**26**	
Height(m)	556	750	1000	1500	2000	3000	4000	5000	

Table 5 Heights of Box-Walls

<u>Other Initial Values</u>

Table 6 shows the initial model setup to obtain the results. Surface source is turned on because as discussed in Section 1.3, snow is a significant HONO source.

Initial Setup	Status
NO Soil emission	Off
Surface source HONO	On
Chemistry timestep (seconds)	300
Internal KPP timestep (seconds)	30
number of diffusions timesteps per chemistry timestep	500

Table 6 Model Initial Setup

2.4 Surface HONO Chemistry Over Snow

In this model, HONO is primarily produced on the ground. Therefore, in the PACT-1D model, complex heterogeneous reactions are applied. Deposition occurs based on the number of molecular collisions with the ground, as well as an uptake coefficient, allowing surface emissions and chemical conversions to be studied at the molecular level. The mechanisms introduced in Section 1.1 are applied in the PACT-1D model (Tuite et al., 2021).

According to reaction R15, every time two NO_2 molecules are consumed, it will produce one HONO molecule and one HNO_3 molecule. According to Trick (2004), the ground NO_2 uptake efficiency is set to 1×10^{-5}.

Photolysis strengthens the conversion from NO_2 to HONO. The enhanced effect is included in the parameterization by Wong et al. (2013). According to Wong et al. (2013), daytime HONO in Houston, TX has a correlation with solar irradiance, which is shown in equation (14):

$$\gamma_{NO_2,photo} = 6 \times 10^{-5} \frac{J_{no_2}^3}{J_{NO_2,noon}^3} \tag{14}$$

Where γ is ground NO_2 uptake coefficient and 6×10^{-5} is maximum reactive coefficient (Tuite et al., 2021).

Combining these two coefficients, we have the deposition rate:

$$v_{d,NO_2} = \frac{1}{4}v(\gamma_{NO_2,dark} + \gamma_{NO_2,photo}) \tag{15}$$

Parameterizing surface absorbed HNO_3 follows the idea of Sarwar et al. (2008) using the following equation (R26):

$$HNO3_{(adv)} + h\nu \rightarrow 0.5HONO_{(ads)} + 0.5NO_{2(ads)} \tag{R26}$$
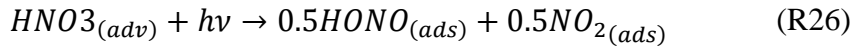
Surface HNO_3 concentration in the model is determined by surface chemistry (discussed above) and deposition. Deposition allows HONO and NO_2 produced in R26 to be released into the lowest layer. In this case, the photolysis rate constant is set to 9 times of gas-phase HNO_3 concentration.

For atmospheric HONO, ground uptake is a main loss especially at night. according to Tuite et al. (2021), HONO will form surface nitrate following a similar mechanism as HNO_4. In this model, we assume all loss HONO and HNO_4 are transformed into nitrate. The uptake coefficients for HONO, HNO_4, and HNO_3 are 0.0001, 0.01, and 0.1, and the molecule number ratio of HNO_3 deposited and HONO emitted to the lowest layer is 1:1 respectively. If HONO

concentration falls below $\sim 1 \times 10^{13}\, molecules/cm^2$, in order to ensure there is enough nitrate to participate in reactions, it will be re-scaled by $\frac{[NO_2^-]}{1 \times 10^{13}}$.

3. RESULT AND DISCUSSION

The PACT-1D model was used to simulate vertical concentration profiles and HONO flux during UBWOS 2014, which were then compared with observational data from UBWOS 2014.

3.1 Concentration Profile

According to Section 2, the UCLA LP-DOAS equipment setup follows the configuration in Figure 2.2. Therefore, based on the vertical profile of boxes in the PACT-1D model, layers 5-8 were used to represent the lower path of observation, layers 5-10 for the medium path, and layers 5-11 for the upper path. The modeled concentration at each box was averaged to the box height and compared to the observation (see Figures 3.1-3.3).
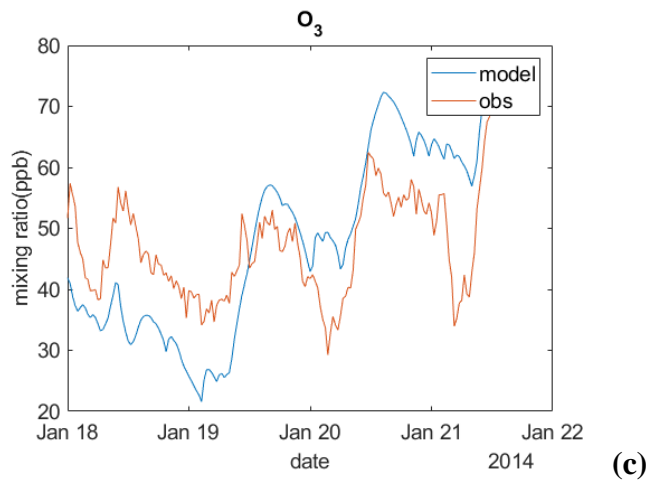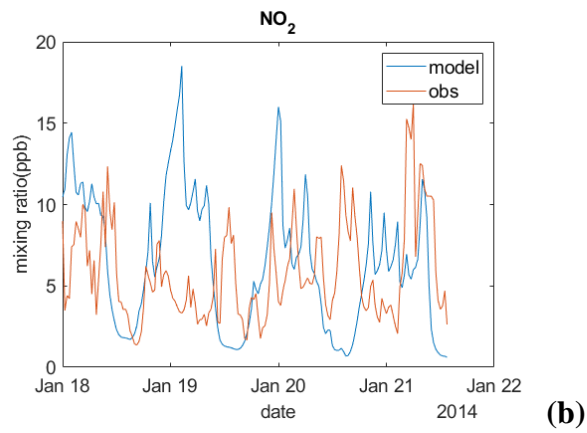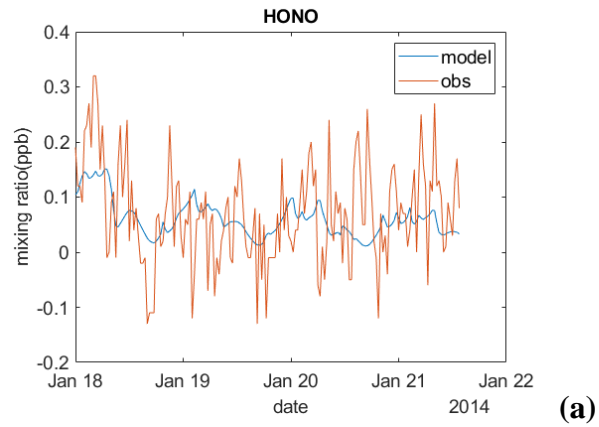
(a)

(b)

(c)

Figure 3.1 Low Path Model vs. Observation of HONO(a), NO_2 (b) and O_3 (c)

(a)

(b)

(c)
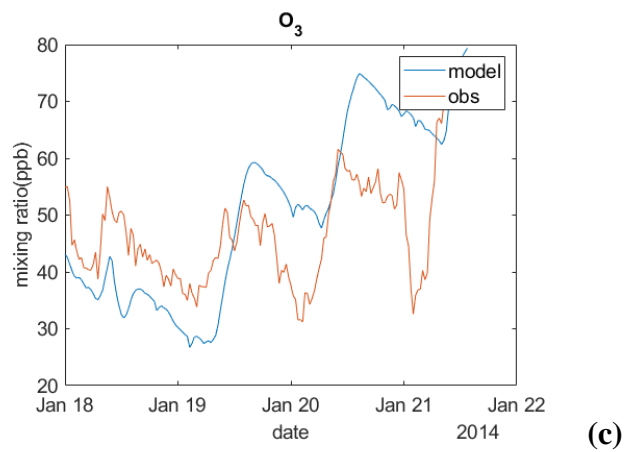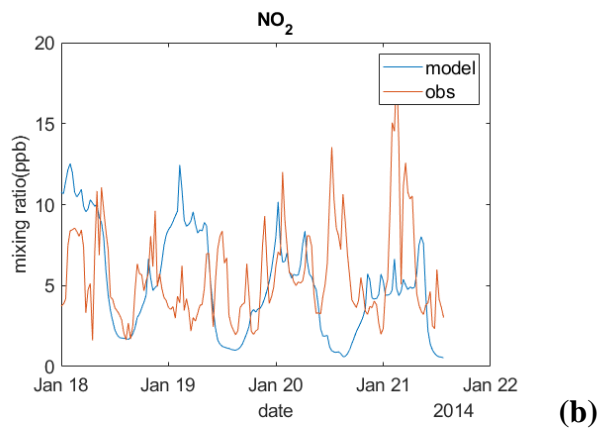
Figure 3.2 Medium Path Model vs. Observation of HONO(a), NO_2 (b) and O_3 (c)

(a)

(b)

(c)

Figure 3.3 Upper Path Model vs. Observation of HONO(a), NO_2 (b) and O_3 (c)

	O₃	NO₂	HONO
Model(ppb)	51.59	4.53	0.044
Observation (LP)(ppb)	47.05	5.42	0.067

Table 7 Mean Mixing Ratio Comparison Between Model and Observation (Low Path)

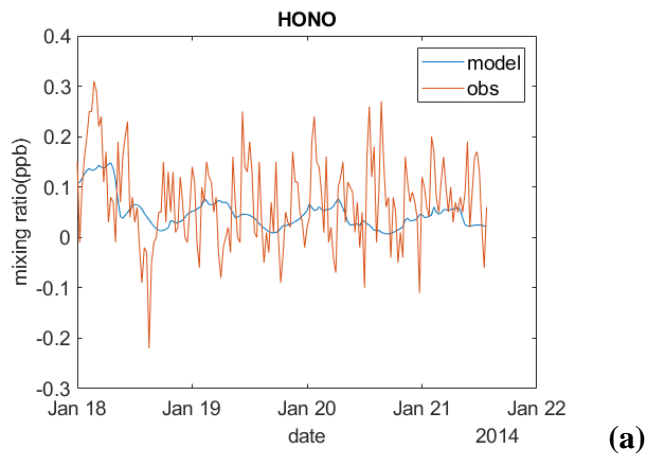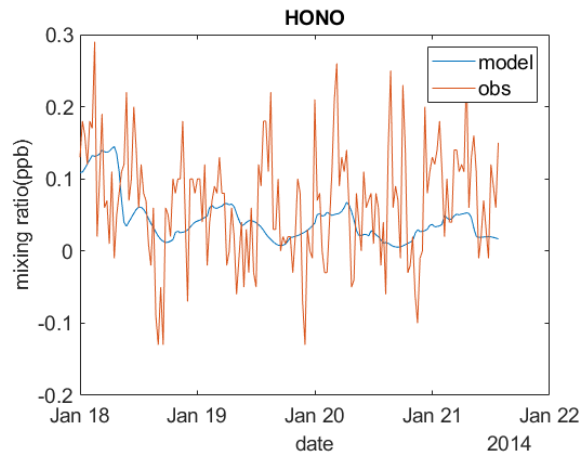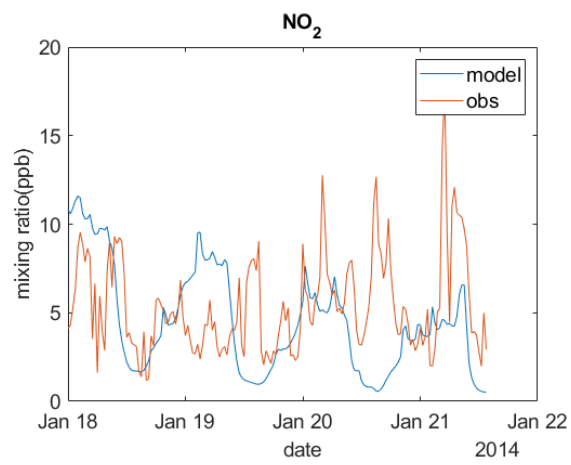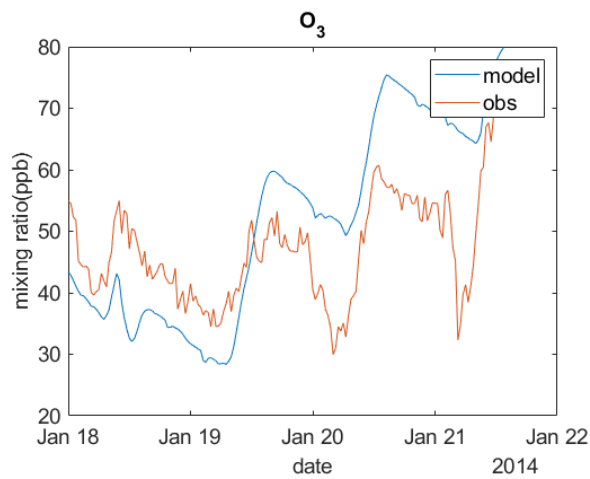Based on the model-observation comparison in Figures 3.1-3.3 and Table 7, the trend and mean mixing ratio of ozone and NO₂ concentrations agreed quite well between observations and model results. However, the ozone mean mixing ratio was slightly overestimated, and the NO₂ and HONO mixing ratios were underestimated.

A constant ozone accumulation was noticed in observation and model. However, the model overestimated ozone accumulation. Additionally, an unusual nighttime accumulation of NO₂ happening at boundary layer was observed in the model; however, this accumulation weakens as the paths become higher. In the low path, the highest peak of the model result reached about 24 ppb, whereas this number decreased to 12 ppb at the upper path.

The observed HONO profile, on the other hand, didn't exhibit a clear trend and shows greater fluctuation than the model results due to some measurement errors, although the quantity of HONO agreed quite well. However, a slight decay of the maximum concentration of HONO in the upper path was observed compared to the lower path, while the observation remained constant. This will be further investigated in the next section.

3.2 Vertical Profile
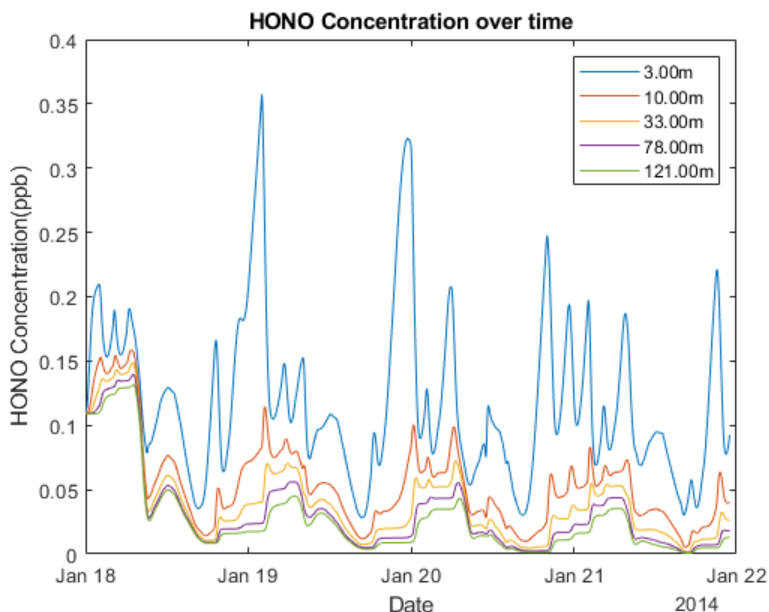
Figure 3.4 HONO Concentration Over Time from Model

Figure 3.4 depicts the model result of HONO concentration over time at different heights, showing an evident accumulation of HONO near the ground (~3m). Specifically, the concentration at 3m is approximately 3-4 times higher compared to the concentration at 10m.

Figure 3.5 provides a clearer view of the vertical profile of species. To enhance clarity regarding the vertical profile of NO_X and HONO at lower levels (0-110m), Figure 3.5 describes this profile. Notably, January 18th is excluded from Figure 3.5 as it resembles more of an initial value of the model rather than a value after chemical reactions have occurred. According to the figure, there was a noticeable accumulation of O_3 in the model, consistent with both model results and observations. Additionally, NO_x and HONO were predominantly concentrated near the ground, corroborating the findings from Figure 3.4.

HONO vertical profile(unit:ppb)

(a)

NO vertical profile(unit:ppb)
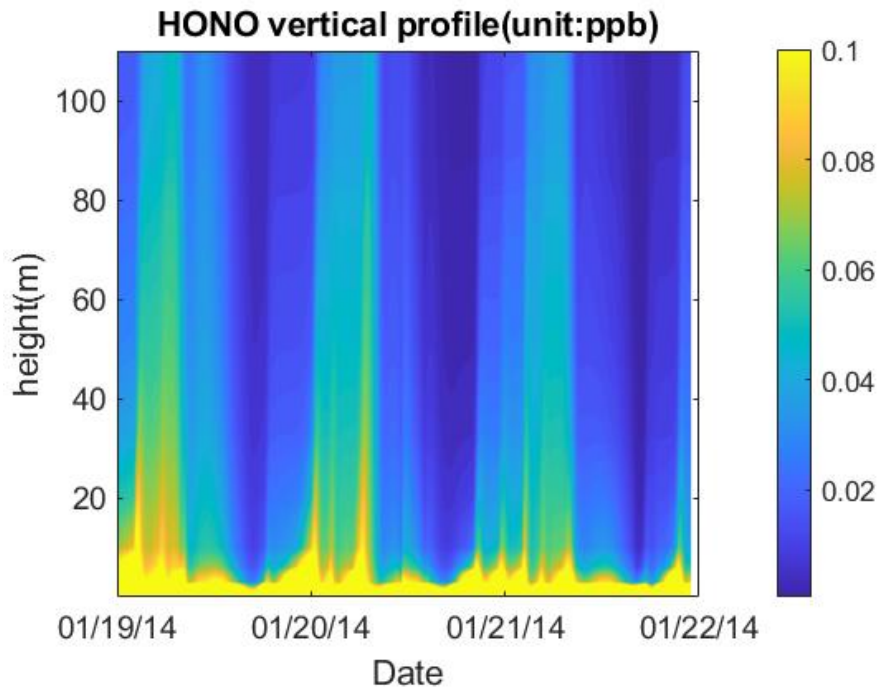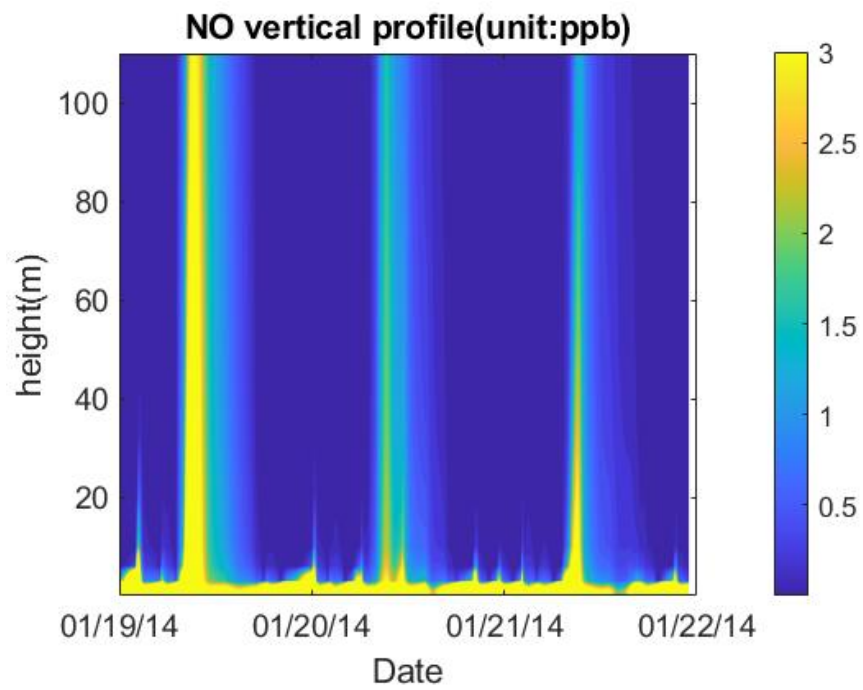
(b)
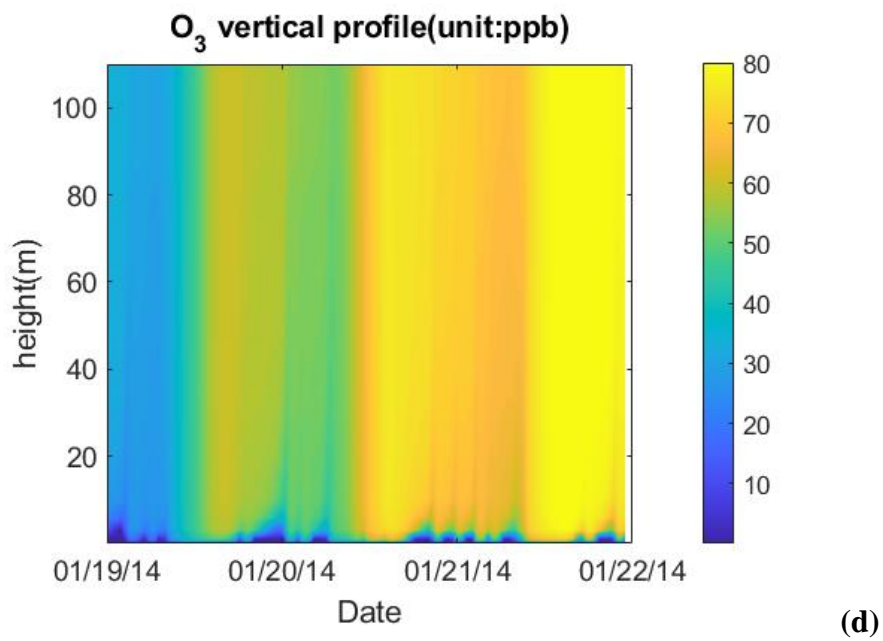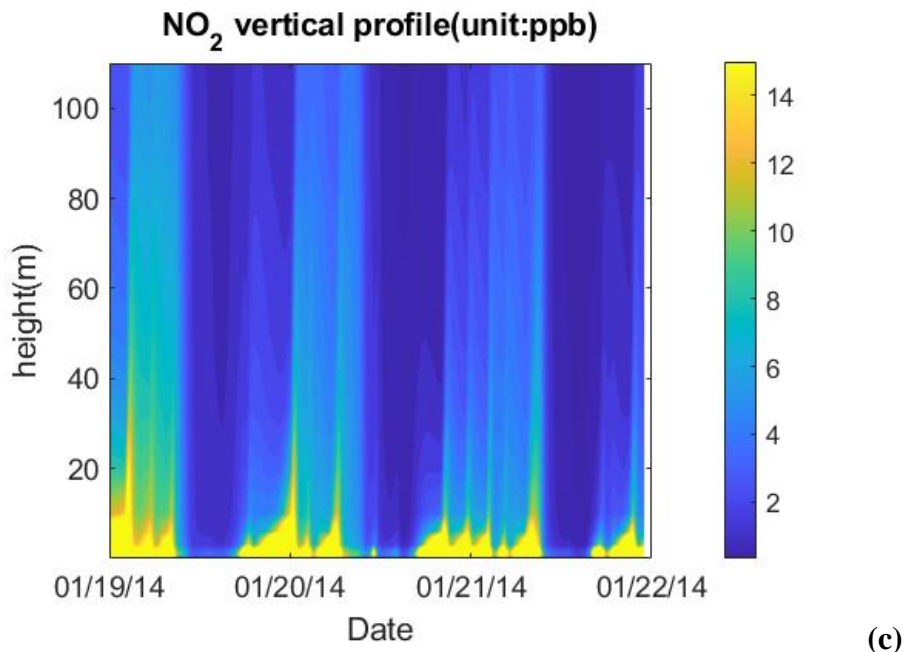
Figure 3.5 Species Vertical Profile near Ground; *HONO(a), NO(b),* NO$_2$ *(c) and* O$_3$ *(d)*

In Figure 3.5, there is a rapid vertical decay of reactive nitrogen species. NO and HONO exhibit high concentrations at around 5m near the ground, but they quickly decay with altitude. Meanwhile, NO$_2$ shows a higher concentration at approximately 10m and also decayed at higher layers.

37

Similar to previous figures, NO and NO$_2$ exhibit cycles that resemble the patterns of the sun, with concentrations rising and falling in correspondence with daylight. Conversely, HONO maintains a relatively stable concentration throughout the observation period.

3.3 HONO Vertical Fluxes

(a)

(b)
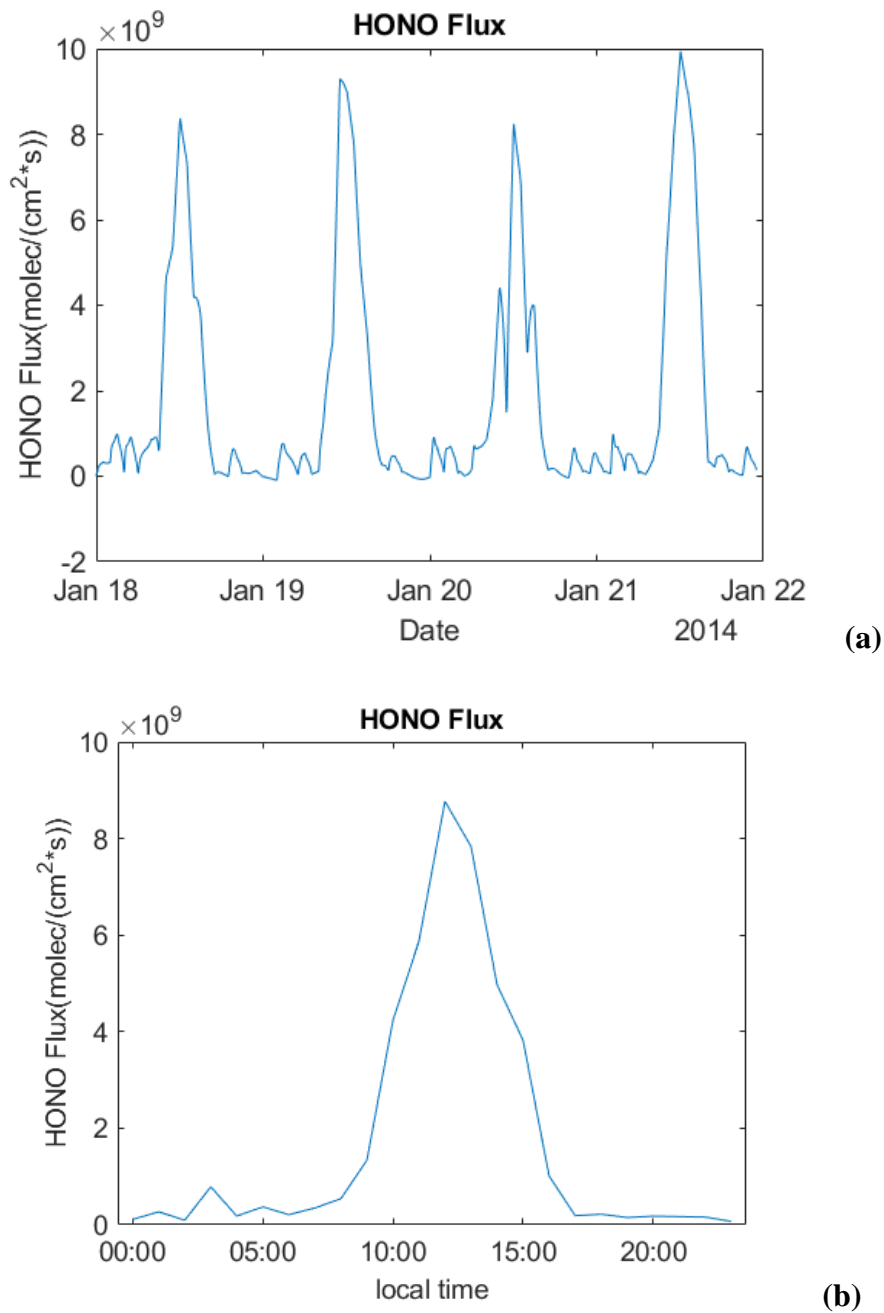
Figure 3.6 HONO Vertical Flux Model Result; a: Full Result b: Diurnal Average

Figure 3.6 illustrates the model results of HONO vertical flux. As depicted in Figure 3.6, the peaks typically occur around 12:00, closely resembling the pattern of the sun cycle. The data for January 20th appears lower due to adverse weather conditions.

The calculated values of the model for HONO fluxes at noon range between 8.37×10^9 and $9.9 \times 10^9 molec\ cm^{-2}s^{-1}$.
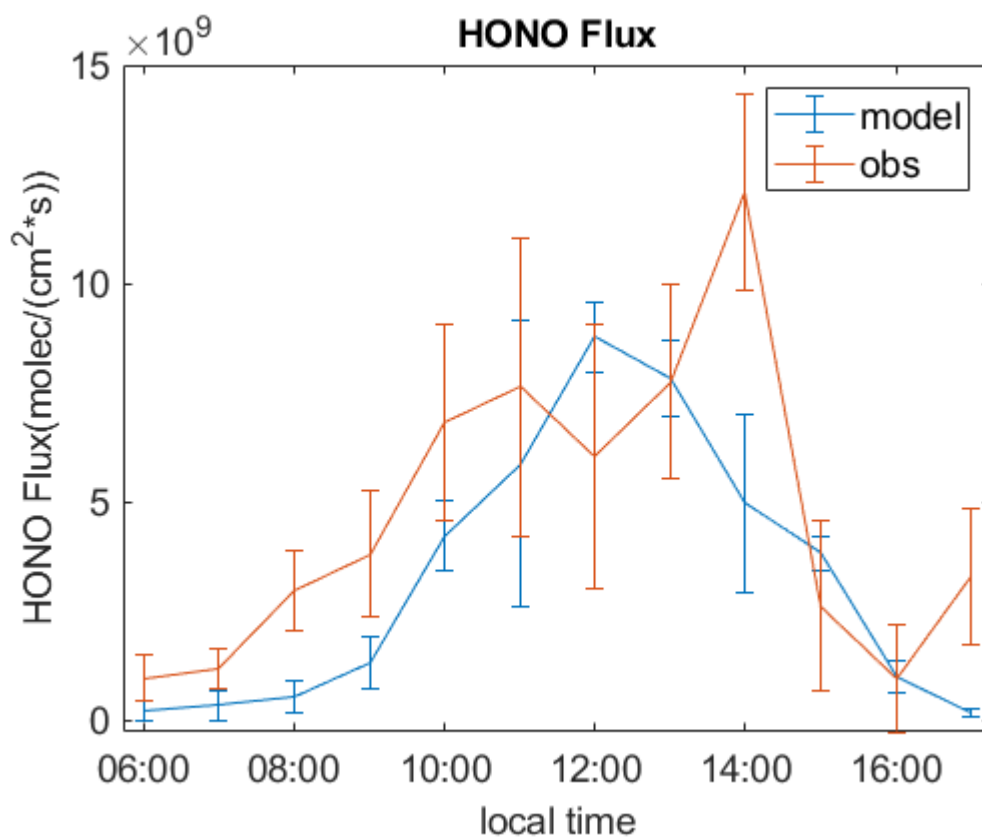
Figure 3.7 HONO Flux Comparison Between Model Result and UBWOS 2014 Observation. Error bars are

standard deviations of hourly flux data.

Figure 3.7 compares the model results with observations from UBWOS 2014 (Tsai, 2016). The model exhibited an earlier peak compared to the observation. Additionally, the model underestimated the HONO vertical flux during the period from 6:00 to 14:00, when the

HONO flux demonstrated an increasing trend. However, as the HONO flux passed its peak, it descended rapidly, leading to an overestimation by the model from 15:00 to 17:00. Overall, under the parameterization mentioned in section 2, the model flux is well explained and show a good agreement with observation in magnitude and shape. The flux also explains HONO emission pattern, which will be discussed in section 4.

4. CONCLUSION AND OUTLOOK

As shown in Fig.3.1-Fig.3.3, the model shows a good agreement on mixing ratios and emission patterns with observation of O_3, NO_2 and HONO. Compared with the studies listed in Section 1.2, the HONO mixing ratio was about 2-10 times larger in both observation and model results. This leads to approximately 10 times larger HONO flux in both model results and observations compared to studies listed in 1.5. This may be due to much higher NO_X emission due from the industrial activities in the Uintah Basin area. According to Tsai (2016), the Uintah Basin boasts over 10,000 oil and gas wells. Additionally, a 500-megawatt coal-based power plant is only 12 miles from the UBWOS site. The energy-based economy produces excessive emissions of NO_X.

When comparing the mixing ratio and the HONO flux, it can be observed that while the HONO flux shows an apparent diurnal cycle (Fig. 3.6a), the HONO mixing ratio wasn't showing the same diurnal cycle (Fig. 3.1a-3.3a). This can be explained by the following reasonings: during the daytime, mixing is more active, and HONO emitted by HNO_3 photolysis is at a higher rate due to sunlight (R16-R19), making a bigger HONO source. At night, there is less mixing in atmosphere, and only NO_2 hydrolysis(R15) is active, resulting in a smaller HONO source. This causes the diurnal pattern of the HONO vertical flux, a pattern possibly similar to that described by Bao et al. (2023).

According to Fig. 3.7b, there is a shift in HONO fluxes between the model results and observation data — the peak of the model result occurs at 12:00 (local time), while the peak of the

41

observation occurs at 14:00 (local time). This may be because the actual K_Z value, as well as J values, peak at 14:00, while the J values output by the TUV model peak at 12:00.

Overall, as HONO formation mechanisms over snow are discussed in Section 1 and implemented in the PACT-1D model to reproduce HONO flux and HONO profile as discussed in Section 2, we can see good agreements between the model results and observation of HONO profile and the HONO flux over snow. To predict HONO and HONO flux over snow even more precisely, the study could be followed by implementation of coupled snow-atmosphere models.

REFERENCES

Acker, K., Febo, A., Trick, S., Perrino, C., Bruno, P., Wiesen, P., Möller, D., Wieprecht, W., Auel, R., Giusto, M., Geyer, A., Platt, U., & Allegrini, I. (2006). Nitrous acid in the urban area of Rome. Atmospheric Environment, 40(17), 3123–3133. https://doi.org/10.1016/j.atmosenv.2006.01.028

Alduchov, O. A., & Eskridge, R. E. (1997). Improved Magnus` form approximation of saturation vapor pressure. Journal of Applied Meteorology and Climatology. https://doi.org/10.2172/548871

Alicke, B., Geyer, A., Hofzumahaus, A., Holland, F., Konrad, S., Pätz, H. W., Schäfer, J., Stutz, J., Volz-Thomas, A., & Platt, U. (2003). Oh formation by HONO photolysis during the Berlioz experiment. Journal of Geophysical Research: Atmospheres, 108(D4). https://doi.org/10.1029/2001jd000579

Amoroso, A., Beine, H. J., Sparapani, R., Nardino, M., & Allegrini, I. (2006). Observation of coinciding Arctic boundary layer ozone depletion and snow surface emissions of nitrous acid. Atmospheric Environment, 40(11), 1949–1956. https://doi.org/10.1016/j.atmosenv.2005.11.027

Bao, F., Cheng, Y., Kuhn, U., Li, G., Wang, W., Kratz, A., Weber, J., Weber, B., Pöschl, U., & Su, H. (2023). Key Role of Equilibrium Hono Concentration over Soil in Quantifying Soil-Atmosphere Hono Fluxes. https://doi.org/10.5194/egusphere-egu23-14862

Barth, M., & Madronich, S. (2021). Tropospheric Ultraviolet and Visible (TUV) Radiation Model. Atmospheric Chemistry Observations & Modeling. https://www2.acom.ucar.edu/modeling/tropospheric-ultraviolet-and-visible-tuv-radiation-model

Beine, H. J., Amoroso, A., Dominé, F., King, M. D., Nardino, M., Ianniello, A., & France, J. L. (2006). Surprisingly small hono emissions from snow surfaces at Browning Pass, Antarctica. Atmospheric Chemistry and Physics, 6(9), 2569–2580. https://doi.org/10.5194/acp-6-2569-2006

Beine, H., Colussi, A. J., Amoroso, A., Esposito, G., Montagnoli, M., & Hoffmann, M. R. (2008). HONO emissions from Snow Surfaces. Environmental Research Letters, 3(4), 045005. https://doi.org/10.1088/1748-9326/3/4/045005

Beine, Harald J., Honrath, R. E., Dominé, F., Simpson, W. R., & Fuentes, J. D. (2002). Nox during background and ozone depletion periods at alert: Fluxes above the snow surface. Journal of Geophysical Research: Atmospheres, 107(D21). https://doi.org/10.1029/2002jd002082

Bond, A. M., Frey, M. M., Kaiser, J., Kleffmann, J., Jones, A. E., & Squires, F. A. (2023). Snowpack Nitrate Photolysis Drives the Summertime Atmospheric Nitrous Acid (HONO) Budget in Coastal Antarctica. https://doi.org/10.5194/egusphere-egu23-5469

Brasseur, G. P., & Jacob, D. J. (2017). Modeling of atmospheric chemistry. Cambridge University Press.

Businger, J. A. (1986). Evaluation of the accuracy with which dry deposition can be measured with current micrometeorological techniques. Journal of Climate and Applied Meteorology, 25(8), 1100–1124. https://doi.org/10.1175/1520-0450(1986)025<1100:eotaww>2.0.co;2

Chen, Q., Edebeli, J., McNamara, S. M., Kulju, K. D., May, N. W., Bertman, S. B., Thanekar, S., Fuentes, J. D., & Pratt, K. A. (2019). Hono, particulate nitrite, and snow nitrite at a midlatitude urban site during wintertime. ACS Earth and Space Chemistry, 3(5), 811–822. https://doi.org/10.1021/acsearthspacechem.9b00023

Chu, L., & Anastasio, C. (2007). Temperature and wavelength dependence of nitrite photolysis in frozen and aqueous solutions. Environmental Science & Technology, 41(10), 3626–3632. https://doi.org/10.1021/es062731q

Dibb, J. E., Arsenault, M., Peterson, M. C., & Honrath, R. E. (2002). Fast nitrogen oxide photochemistry in Summit, greenland snow. Atmospheric Environment, 36(15–16), 2501–2511. https://doi.org/10.1016/s1352-2310(02)00130-9

Döppenschmidt, A., & Butt, H.-J. (2000). Measuring the thickness of the liquid-like layer on ice surfaces with atomic force microscopy. Langmuir, 16(16), 6709–6714. https://doi.org/10.1021/la990799w

Farina, G., Spataro, F., De Lorenzo, A., & Lukaski, H. (2017). Correction: Farina, G.L., et al. A smartphone application for personal assessments of body composition and phenotyping. sensors 2016, 16, 2163. Sensors, 17(3), 434. https://doi.org/10.3390/s17030434

FUCHS, N. A., & SUTUGIN, A. G. (1971). High-dispersed aerosols. Topics in Current Aerosol Research, 1. https://doi.org/10.1016/b978-0-08-016674-2.50006-6

George, C., Strekowski, R. S., Kleffmann, J., Stemmler, K., & Ammann, M. (2005). Photoenhanced uptake of gaseous NO2 on solid organic compounds: A photochemical source of Hono? Faraday Discussions, 130, 195. https://doi.org/10.1039/b417888m

Gligorovski, S., Strekowski, R., Barbati, S., & Vione, D. (2015). Environmental implications of hydroxyl radicals (•oh). Chemical Reviews, 115(24), 13051–13092. https://doi.org/10.1021/cr500310b

Goliff, W. S., Stockwell, W. R., & Lawson, C. V. (2013). The regional atmospheric chemistry mechanism, version 2. Atmospheric Environment, 68, 174–185. https://doi.org/10.1016/j.atmosenv.2012.11.038

Grannas, A. M., Jones, A. E., Dibb, J., Ammann, M., Anastasio, C., Beine, H. J., Bergin, M., Bottenheim, J., Boxe, C. S., Carver, G., Chen, G., Crawford, J. H., Dominé, F, Frey, M. M., Guzmán, M. I., Heard, D. E., Helmig, D., Hoffmann, M. R., Honrath, R. E., … Zhu, T. (2007). An overview of snow photochemistry: Evidence, mechanisms and impacts. Atmospheric Chemistry and Physics, 7(16), 4329–4373. https://doi.org/10.5194/acp-7-4329-2007

Grannas, Amanda M, Shepson, P. B., Guimbaud, C., Sumner, A. L., Albert, M., Simpson, W., Dominé, F., Boudries, H., Bottenheim, J., Beine, H. J., Honrath, R., & Zhou, X. (2002). A study of photochemical and physical processes affecting carbonyl compounds in the Arctic

atmospheric boundary layer. Atmospheric Environment, 36(15–16), 2733–2742. https://doi.org/10.1016/s1352-2310(02)00134-6

Honrath, R. E., Lu, Y., Peterson, M. C., Dibb, J. E., Arsenault, M. A., Cullen, N. J., & Steffen, K. (2002). Vertical Fluxes of NOx, Hono, and HNO3 above the snowpack at Summit, Greenland. Atmospheric Environment, 36(15–16), 2629–2640. https://doi.org/10.1016/s1352-2310(02)00132-2

Honrath, R. E., Peterson, M. C., Guo, S., Dibb, J. E., Shepson, P. B., & Campbell, B. (1999). Evidence of nox production within or upon ice particles in the Greenland snowpack. Geophysical Research Letters, 26(6), 695–698. https://doi.org/10.1029/1999gl900077

Hood, J. W. (1976). Characteristics of aquifers in the northern Uinta Basin area, Utah and Colorado. Open-File Report. https://doi.org/10.3133/ofr76323

Jacobi, H.-W., & Hilker, B. (2007). A mechanism for the photochemical transformation of nitrate in snow. Journal of Photochemistry and Photobiology A: Chemistry, 185(2–3), 371–382. https://doi.org/10.1016/j.jphotochem.2006.06.039

Jacobi, H.-W., Bales, R. C., Honrath, R. E., Peterson, M. C., Dibb, J. E., Swanson, A. L., & Albert, M. R. (2004). Reactive trace gases measured in the interstitial air of surface snow at Summit, Greenland. Atmospheric Environment, 38(12), 1687–1697. https://doi.org/10.1016/j.atmosenv.2004.01.004

Kirchstetter, T. W., Harley, R. A., & Littlejohn, D. (1996). Measurement of nitrous acid in motor vehicle exhaust. Environmental Science & Technology, 30(9), 2843–2849. https://doi.org/10.1021/es960135y

Kleffmann, J., Heland, J., Kurtenbach, R., Lorzer, J., & Wiesen, P. (2002). A new instrument (LOPAP) for the detection of nitrous acid (HONO). Environmental Science and Pollution Research, 48–54.

Kleffmann, Jörg, Gavriloaiei, T., Hofzumahaus, A., Holland, F., Koppmann, R., Rupp, L., Schlosser, E., Siese, M., & Wahner, A. (2005). Daytime formation of nitrous acid: A major source of oh radicals in a forest. Geophysical Research Letters, 32(5). https://doi.org/10.1029/2005gl022524

Kleffmann, Jörg. (2007). Daytime sources of nitrous acid (HONO) in the atmospheric boundary layer. ChemPhysChem, 8(8), 1137–1144. https://doi.org/10.1002/cphc.200700016

Kramer, L. J., Crilley, L. R., Adams, T. J., Ball, S. M., Pope, F. D., & Bloss, W. J. (2019). Nitrous Acid (HONO) Emissions under Real-World Driving Conditions from Vehicles in a UK Road Tunnel. https://doi.org/10.5194/acp-2019-1070

Kurtenbach, R., Becker, K. H., Gomes, J. A. G., Kleffmann, J., Lörzer, J. C., Spittler, M., Wiesen, P., Ackermann, R., Geyer, A., & Platt, U. (2001). Investigations of emissions and heterogeneous formation of HONO in a road traffic tunnel. Atmospheric Environment, 35(20), 3385–3394. https://doi.org/10.1016/s1352-2310(01)00138-8

LeBaron, B. (2017). Final 2014 O&G Emissions Table. 2014 Air Agencies Oil and Gas Emissions Inventory: Uinta Basin. https://deq.utah.gov/air-quality/2014-air-agencies-oil-and-gas-emissions-inventory-uinta-basin

Legrand, M., Preunkert, S., Frey, M., Bartels-Rausch, Th., Kukui, A., King, M. D., Savarino, J., Kerbrat, M., & Jourdain, B. (2014). Large mixing ratios of atmospheric nitrous acid (HONO) at Concordia (East Antarctic Plateau) in summer: A strong source from surface snow? Atmospheric Chemistry and Physics, 14(18), 9963–9976. https://doi.org/10.5194/acp-14-9963-2014

Meller, R., & Moortgat, G. K. (2000). Temperature dependence of the absorption cross sections of formaldehyde between 223 and 323 K in the wavelength range 225–375 nm. Journal of Geophysical Research: Atmospheres, 105(D6), 7089–7101. https://doi.org/10.1029/1999jd901074

Michoud, V., Colomb, A., Borbon, A., Miet, K., Beekmann, M., Camredon, M., Aumont, B., Perrier, S., Zapf, P., Siour, G., Ait-Helal, W., Afif, C., Kukui, A., Furger, M., Dupont, J. C., Haeffelin, M., & Doussin, J. F. (2014). Study of the unknown hono daytime source at a European suburban site during the MEGAPOLI summer and Winter Field Campaigns. Atmospheric Chemistry and Physics, 14(6), 2805–2822. https://doi.org/10.5194/acp-14-2805-2014

Min, K.-E., Washenfelder, R. A., Dubé, W. P., Langford, A. O., Edwards, P. M., Zarzana, K. J., Stutz, J., Lu, K., Rohrer, F., Zhang, Y., & Brown, S. S. (2016). A broadband cavity enhanced absorption spectrometer for aircraft measurements of glyoxal, methylglyoxal, nitrous acid,

nitrogen dioxide, and water vapor. Atmospheric Measurement Techniques, 9(2), 423–440. https://doi.org/10.5194/amt-9-423-2016

Oswald, R., Behrendt, T., Ermel, M., Wu, D., Su, H., Cheng, Y., Breuninger, C., Moravek, A., Mougin, E., Delon, C., Loubet, B., Pommerening-Röser, A., Sörgel, M., Pöschl, U., Hoffmann, T., Andreae, M. O., Meixner, F. X., & Trebs, I. (2013). HONO emissions from soil bacteria as a major source of atmospheric reactive nitrogen. Science, 341(6151), 1233–1235. https://doi.org/10.1126/science.1242266

Paulson, S. E., Chung, M. Y., & Hasson, A. S. (1999). Oh radical formation from the gas-phase reaction of ozone with terminal alkenes and the relationship between structure and mechanism. The Journal of Physical Chemistry A, 103(41), 8125–8138. https://doi.org/10.1021/jp991995e

Pinto, J. P., Dibb, J., Lee, B. H., Rappenglück, B., Wood, E. C., Levy, M., Zhang, R. -Y., Lefer, B., Ren, X. -R., Stutz, J., Tsai, C., Ackermann, L., Golovko, J., Herndon, S. C., Oakes, M., Meng, Q. -Y., Munger, J. W., Zahniser, M., & Zheng, J. (2014). Intercomparison of field measurements of nitrous acid (HONO) during the sharp campaign. Journal of Geophysical Research: Atmospheres, 119(9), 5583–5601. https://doi.org/10.1002/2013jd020287

Platt, U., & Stutz, J. (2008). Differential absorption spectroscopy. Physics of Earth and Space Environments, 135–174. https://doi.org/10.1007/978-3-540-75776-4_6

Roberts, J. M., Veres, P., Warneke, C., Neuman, J. A., Washenfelder, R. A., Brown, S. S., Baasandorj, M., Burkholder, J. B., Burling, I. R., Johnson, T. J., Yokelson, R. J., & de Gouw,

J. (2010). Measurement of hono, HNCO, and other inorganic acids by negative-ion proton-transfer chemical-ionization mass spectrometry (NI-pt-CIMS): Application to biomass burning emissions. Atmospheric Measurement Techniques, 3(4), 981–990. https://doi.org/10.5194/amt-3-981-2010

Rohrer, F., Bohn, B., Brauers, T., Brüning, D., Johnen, F.-J., Wahner, A., & Kleffmann, J. (2005). Characterisation of the photolytic hono-source in the atmosphere simulation chamber Saphir. Atmospheric Chemistry and Physics, 5(8), 2189–2201. https://doi.org/10.5194/acp-5-2189-2005

Rohrer, Franz, & Berresheim, H. (2006). Strong correlation between levels of tropospheric hydroxyl radicals and solar ultraviolet radiation. Nature, 442(7099), 184–187. https://doi.org/10.1038/nature04924

Sandu, A., & Sander, R. (2006). Technical note: Simulating chemical systems in Fortran90 and MATLAB with the kinetic preprocessor KPP-2.1. Atmospheric Chemistry and Physics, 6(1), 187–195. https://doi.org/10.5194/acp-6-187-2006

Sarwar, G., Roselle, S. J., Mathur, R., Appel, W., Dennis, R. L., & Vogel, B. (2008). A comparison of CMAQ HONO predictions with observations from the Northeast Oxidant and particle study. Atmospheric Environment, 42(23), 5760–5770. https://doi.org/10.1016/j.atmosenv.2007.12.065

Spataro, F., Ianniello, A., Salvatori, R., Nardino, M., Esposito, G., & Montagnoli, M. (2016). Sources of atmospheric nitrous acid (HONO) in the European high arctic. Rendiconti Lincei, 28(1), 25–33. https://doi.org/10.1007/s12210-016-0568-9

Stanhill, G. (1969). A simple instrument for the field measurement of turbulent diffusion flux. Journal of Applied Meteorology, 8(4), 509–513. https://doi.org/10.1175/1520-0450(1969)008<0509:asiftf>2.0.co;2

Stoeckenius, T. (2015). Final Report 2014 Uinta Basin Winter Ozone Study. https://documents.deq.utah.gov/air-quality/planning/air-quality-policy/DAQ-2015-021002.pdf

Telford, J. W., & Businger, J. A. (1986). Comments on "Von k´rm´n's constant in atmospheric boundary layer flow: Reevaluated." Journal of the Atmospheric Sciences, 43(19), 2127–2130. https://doi.org/10.1175/1520-0469(1986)043<2127:cokcia>2.0.co;2

Trick, S. (2004). Formation of nitrous acid on urban surfaces—A physical chemical perspective. (Unpublished Doctoral Dissertation).

Tsai, C. (2016). Nitrous Acid Formation and Chemistry over Soil and Snow in a Polluted Rural Area. (Doctoral Dissertation, UCLA).

Tuite, K., Thomas, J. L., Veres, P. R., Roberts, J. M., Stevens, P. S., Griffith, S. M., Dusanter, S., Flynn, J. H., Ahmed, S., Emmons, L., Kim, S., Washenfelder, R., Young, C., Tsai, C., Pikelnaya, O., & Stutz, J. (2021). Quantifying nitrous acid formation mechanisms using measured vertical profiles during the CalNex 2010 campaign and 1D Column modeling.

Journal of Geophysical Research: Atmospheres, 126(13).
https://doi.org/10.1029/2021jd034689

VandenBoer, T. C., Young, C. J., Talukdar, R. K., Markovic, M. Z., Brown, S. S., Roberts, J. M., & Murphy, J. G. (2014). Nocturnal loss and daytime source of nitrous acid through reactive uptake and displacement. Nature Geoscience, 8(1), 55–60. https://doi.org/10.1038/ngeo2298

Wong, K. W., Tsai, C., Lefer, B., Grossberg, N., & Stutz, J. (2013). Modeling of daytime hono vertical gradients during sharp 2009. Atmospheric Chemistry and Physics, 13(7), 3587–3601. https://doi.org/10.5194/acp-13-3587-2013

Wong, K. W., Tsai, C., Lefer, B., Haman, C., Grossberg, N., Brune, W. H., Ren, X., Luke, W., & Stutz, J. (2012). Daytime hono vertical gradients during sharp 2009 in Houston, TX. Atmospheric Chemistry and Physics, 12(2), 635–652. https://doi.org/10.5194/acp-12-635-2012

Wu, T., Chen, W., Fertein, E., Cazier, F., Dewaele, D., & Gao, X. (2011). Development of an open-path incoherent broadband cavity-enhanced spectroscopy based instrument for simultaneous measurement of HONO and no2 in ambient air. Applied Physics B, 106(2), 501–509. https://doi.org/10.1007/s00340-011-4818-3

Zhou, X., Civerolo, K., Dai, H., Huang, G., Schwab, J., & Demerjian, K. (2002). Summertime nitrous acid chemistry in the atmospheric boundary layer at a rural site in New York State. Journal of Geophysical Research: Atmospheres, 107(D21). https://doi.org/10.1029/2001jd001539

Zhou, X., Huang, G., Civerolo, K., Roychowdhury, U., & Demerjian, K. L. (2007). Summer-time observations of Hono, HCHO, and O3 at the summit of Whiteface Mountain, New York. Journal of Geophysical Research: Atmospheres, 112(D8). https://doi.org/10.1029/2006jd007256